Additive Manufacturing Letters 17 (2026) 100363

Contents lists available at ScienceDirect

Additive Manufacturing Letters

journal homepage: www.elsevier.com/locate/addlet

Short Communication

Cold spray additively manufactured pure iron for magnetic applications

Abhinav Anand [a,b,*], Ondřej Kovářík [c], Pavel Ctibor [b], Zahra Arabgol [d], Levke Wiehler [d], Frank Gärtner [d], Thomas Klassen [d], Jan Cizek [b]

[a] Department of Mechanical Engineering, Politecnico di Milano, Milano, Italy
[b] Institute of Plasma Physics of the Czech Academy of Sciences, Prague, Czech Republic
[c] Faculty of Nuclear Science and Physical Engineering, Czech Technical University, Prague, Czech Republic
[d] Helmut Schmidt University, Hamburg, Germany

ARTICLE INFO

Keywords:
Cold spray additive manufacturing
Component repair
Fatigue crack growth rate
Fracture toughness
Electromagnetic behavior

ABSTRACT

Pure iron powder combines excellent plastic deformability under a high-velocity impact with high magnetizability and permeability, making it an economical candidate for cold spray additive manufacturing (CSAM) and repairs in magnetic applications. This work explores the fracture mechanics and electromagnetic (EM) properties of CSAM pure iron deposited using cheaper nitrogen as the process gas at temperatures of 900 °C and 1000 °C, achieving relative densities of 97.3 % and 98.0 %, respectively. The deposits exhibited an ultimate tensile strength greater than 250 MPa and elongation to fracture of less than 0.3 %, a behavior consistent with the characteristic results of as-sprayed CSAM deposits. The fatigue crack growth rate analyses showed the propagation being faster than in wrought iron through different mechanisms: trans-particle crack propagation near the threshold stress intensity factor, and inter-particle decohesion at higher loads. The EM testing indicated that CSAM pure iron saturated at a lower induction and had lower permeability than wrought low-carbon steel, while its coercivity and hysteresis losses were higher, and electrical resistivity was similar. Despite the lower mechanical and magnetic performance, CSAM pure iron or similarly deformable ferritic alloys can meet the requirements for low-field, low-frequency, or direct-current applications, and provide a route for direct near-net-shape additive manufacturing or in-situ repair of magnetic components without scraping existing parts.

1. Introduction

Owing to their high saturation induction, low coercivity, and excellent initial permeability, specific ferritic alloys are well established as soft magnetic materials [1]. Common ferritic grades include Fe-Si electrical steel with 1 to 3.5 wt. % Si and Fe-Al with 2 to 6 wt. % Al. The addition of alloying element increases resistivity, suppresses eddy current losses, and improves magnetic efficiency, so these alloys are used in transformers and motor cores, magnetic shielding, and actuators. Ferritic stainless steels, such as Fe-Cr with 11 to 18 wt. % Cr are used where corrosion resistance is needed, for example, in appliance housings and exhaust systems [2]. High-performance ferritic steel coatings are already used for efficient induction heating on aluminum cookware base plates [3].

With respect to general properties, mechanical deformation behavior, and manufacturing routes, pure iron can be considered a model system, allowing the derivation of some general features concerning the behavior of ferritic alloys. Conventional casting and machining of pure iron parts result in long lead times and high costs for complex or miniaturized geometries. Powder metallurgy (PM) techniques, and fusion-based additive manufacturing (AM), such as laser powder bed fusion (L-PBF), have therefore been explored to produce near-net-shape pure iron components [4,5]. Cold spray additive manufacturing (CSAM) is a solid-state process that uses supersonic metal powder impacts to build or repair parts layer-by-layer without melting. Compared to L-PBF and PM, CSAM offers additional advantages, including rapid solid-state deposition with reduced porosity and negligible heat-induced effects, such as oxidation and heat-affected zones. The limitations of the method include the dependence of deposition on sufficient particle plasticity and challenges in geometric accuracy for large deposits, such as local thickness variations that may require toolpath planning and post-machining [6,7]. Previously, Hammouda et al. cold-sprayed Fe-Ni alloy to produce dense, well-bonded coatings for ferromagnetic applications with porosity below 1 % and demonstrated

* Corresponding author at: Department of Mechanical Engineering, Politecnico di Milano, Milano, Italy.
E-mail address: abhinavanand@polimi.it (A. Anand).

https://doi.org/10.1016/j.addlet.2026.100363
Received 23 November 2025; Received in revised form 1 February 2026; Accepted 1 February 2026
Available online 2 February 2026

that deposits processed with coarser powder (Dv50 ~ 35 μm) exhibit higher magnetic saturation and lower coercivity than finer particle (Dv50 ~ 13 μm) counterparts [8]. In the case of pure iron, CSAM further offers an unprecedented capability for in-situ repair of components without thermal damage to adjacent structures, and the deposition of magnetic-shielding coatings [9,10]. However, no study has been reported on the magnetic properties of CSAM pure iron. In this study, pure iron serves as the body-centered cubic (BCC) magnetic baseline for establishing CSAM process-structure-property relations and for guiding the development of iron-based alloys for magnetic coating deposition in subsequent work.

Understanding the static and fatigue performance of cold-sprayed metals is critical to ensure the durability of repaired or newly fabricated components. In our previous study [11], we conducted a comprehensive mechanical and fatigue properties study of CSAM pure nickel, copper, aluminum, and titanium using a unified rectangular bar specimen geometry. However, no equivalent investigation exists for CSAM pure iron or other bcc metals. In this work, the same approach was applied to evaluate static stress-strain behavior, fatigue crack growth rates, and fracture toughness of pure iron CSAM deposits according to Herbert's procedure [12], the ASTM E1820 [13] and E647 standards [14], respectively. The mechanical behavior was then correlated with microstructural and fractographic observations to understand anisotropy and crack growth mechanisms. Then, magnetic behavior was evaluated by measuring direct-current (DC) B-H hysteresis loops (magnetic flux density *B* versus field strength *H*). Finally, the electrical conductivity of the CSAM deposits was analyzed.

2. Materials and methods

2.1. Sample fabrication and microstructure evaluation

Water-atomized iron powder (Höganäs AHC100.29, 99.7 % purity) was used as a feedstock material. The powder morphology was evaluated using an EVO MA 15 scanning electron microscope (SEM, Carl Zeiss SMT, Germany) in backscatter electron (BSE) mode. The powder size distribution was measured by a laser diffraction method using Mastersizer 3000 (Malvern, UK). Fig. 1 shows the irregular morphology of the powder particles typical for the water-atomization process, with adherent sub-sized satellites. In CSAM, such irregular water-atomized powders can still achieve coating properties comparable to spherical powders, while offering a lower-cost feedstock option [15]. The particle sizes were characterized in terms of number density distribution functions. The powder had D10, D50, and D90 decile values of 8.6 μm, 18.9 μm, and 42.7 μm, respectively, placing its particle size distribution within the recommended range for cold spray feedstock [16].

Cold spraying was performed by using the ISS 5/11 high-pressure cold spray system (Impact Innovations GmbH, Germany) with nitrogen as propellant gas at a pressure of 5 MPa. Two deposits were created with process gas temperatures of 900 °C and 1000 °C, respectively, and the resulting deposits were referred to as CS900 and CS1000. All other parameters were kept constant, i.e., powder feed of approximately 36 g/min, gun traverse speed of 250 mm/s, nozzle pass spacing of 2 mm, and standoff distance of 60 mm. This large standoff distance is consistent with parameter sets reported for the Impact Innovations 5/11 high-pressure CSAM [17], and avoiding the very short standoff regime where bow-shock effects can reduce deposition efficiency [18]. Deposits with a thickness of 7 mm were prepared on grit-blasted 1050A-H24 aluminum substrates with dimensions of 100 × 100 × 10 mm^3, requiring 45 torch passes for CS900 and 50 for CS1000.

From the deposits, metallography samples for electron backscatter diffraction (EBSD) and microstructure analysis were prepared by progressive grinding and polishing, with the final step involving twelve hours of vibratory polishing in colloidal silica using a VibroMet 2 (Buehler, USA). SEM micrographs of the cross-sections were acquired in electron-channeling contrast imaging (ECCI) mode using a JSM-IT500HR SEM (JEOL, Tokyo, Japan). EBSD analyses were performed using a Velocity camera (EDAX LLC, Pleasanton, CA, USA) and OIM software. The inverse pole figure (IPF) maps were obtained from the same specimens previously used for fatigue crack growth tests.

The unified rectangular bars of dimension (32 × 4 × 3 mm^3) were extracted from the deposits using electrical discharge machining (EDM) in L-S, L-T, T-S, and T-L orientations defined in ASTM E399 [19], where L denotes the nozzle long-scan direction, T the nozzle pass spacing

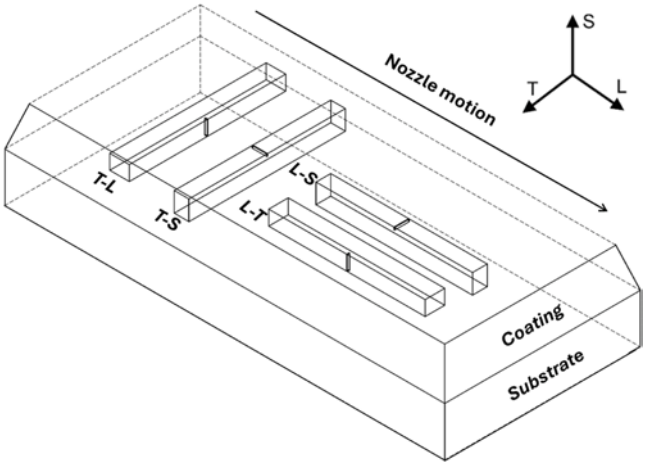

Fig. 2. Orientation convention for CSAM specimens where L, T, and S represent nozzle long-scan, nozzle pass spacing, and build directions, respectively.

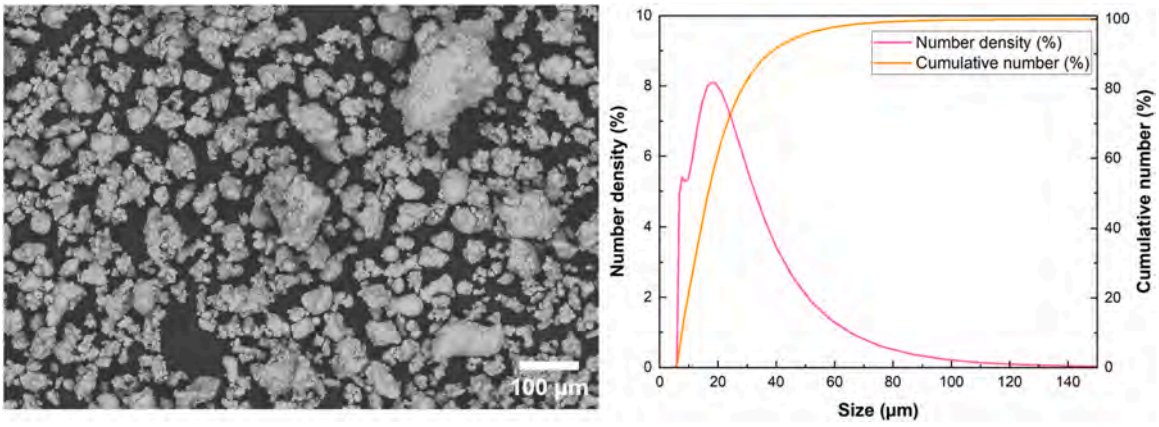

Fig. 1. Irregular morphology of the feedstock pure iron powder and its particle size distribution curve.

direction, and S the torch-axis (build-up) direction, as shown in Fig. 2. For fatigue crack growth rate (FCGR) analyses, the rectangular bars were notched 0.5 mm in their middle using a low-speed diamond saw and tested using the resonance-bending apparatus described in [11]. Specimen orientations were reported using a two-letter code with the first letter denoting the long axis of the bar (L, T, or S), and the second representing the crack-propagation direction. The samples were polished to remove any surface irregularities, and one major face (32×4 mm^2) was etched in Nital to create the high-contrast pattern required for digital image correlation (DIC).

2.2. Static mechanical properties testing

Stress-strain behavior in tension was derived from four-point bending tests using the experimental setup detailed in [20]. Surface deformations were tracked using a monochrome, telecentric-lens camera and analyzed in Ncorr DIC software [21]. DIC measurements were performed on the polished 32×4 mm^2 side face in the region of constant bending moment between the inner loading pins.

The relative density of the two deposits was measured using Archimedes' principle and reported as the average of four samples. Each specimen was weighed in air (W_a) and while fully submerged in water (W_w), which provided the displaced water volume, and then the bulk density was measured. Specimens were then removed, surface dried, and weighed again in air (W_i). The small mass increase (W_i - W_a) corresponded to water entering surface-connected pores and was taken as the open porosity. Using the known pore-free density of pure iron (7.86 g/cm^3) together with the bulk density from Archimedes' test, the total porosity was obtained, while closed porosity was taken as total minus open. Porosity was also quantified by image analysis on metallographic cross-sections. The polished 2D sections were prepared in the L-S, L-T, and T-S orientations and imaged by SEM in backscattered electron mode. For each orientation, images were analyzed individually using ImageJ software [22]. Pores were segmented by grayscale thresholding, and the pore area fraction was calculated.

2.3. Fatigue and fracture mechanics testing

Cyclic loading was applied in pure bending at $R \sim -1$. The differential compliance technique was used to measure the crack length (a) in real time, which has been described in detail in [23]. A rate-controlled algorithm first extended the crack to $a = 1.1$ mm while reducing da/dN from $\sim 1 \times 10^{-10}$ m/cycle to 3×10^{-11} m/cycle. FCGR data were then collected as the da/dN was increased exponentially, and the test was stopped at $a \sim 2$ mm when da/dN reached $\sim 1 \times 10^{-6}$ m/cycle. The tests were repeated using two specimens per orientation, and while the average curves are present in this paper, the individual replicate FCGR datasets are provided in the available Supplementary material document.

Fracture toughness was evaluated on the fatigue pre-cracked notched specimens using a three-point bending setup [20], with a linear variable differential transformer (LVDT) sensor recording the load-line displacement. Crack length data were obtained from unloading compliance for R-curve construction and determination of J_{IC} (the critical value of the J-integral at stable crack-growth initiation), which was converted to fracture toughness (K_{IC}) using the formula $K_{IC} = \sqrt{\frac{E \cdot J_{IC}}{1-\nu^2}}$, where E and ν represent the elastic modulus and Poisson's ratio. The fracture surfaces were then examined by SEM using the JSM-IT500HR SEM (JEOL, Tokyo, Japan).

2.4. Magnetic and electrical performance evaluations

The hysteresis curves and the initial magnetization runs were analyzed by using a permeameter (in-house produced by the Faculty of Electrical Engineering of the Czech Technical University) with maximum magnetic field intensity H up to 4 kA/m. The magnetization period was set to approximately 30 s. Cylindrical samples with a 5 mm diameter and 100 mm length were cut out using EDM with their longitudinal axes aligned with the L direction and inserted into the ballistic coil of the magnetic yoke. The CS1000 deposit was selected as the best representative as it had the lowest porosity among the as-sprayed deposits, thereby minimizing the influence of voids and unbonded regions on the measured magnetic response. The pole pieces of the magnetic yoke were pressed against the faces of the sample using a screw. Before measuring, it was necessary to demagnetize the sample in an alternating magnetic field. The calculation of specific hysteresis losses assumed that there was a quasi-static hysteresis loop (suppression of eddy losses). A cold-drawn low-carbon steel bar, grade EN 10,025–2 S235JR with C $\leq$ 0.17 wt. %, P $\leq$ 0.045 wt. %, S $\leq$ 0.045 wt. %, N $\leq$ 0.007 wt. %, and Fe $\geq$ 99.73 wt. % (cf. the 99.7 % powder purity) was used as the ferromagnetic reference material. Electric DC resistivity was measured by a four-point technique at a current of 1 A, always 5 plus 5 measurements with opposite polarity to compensate for thermoelectric effects. The comparative method was used, measuring the voltage on the sample and on the standard that are connected in series to ensure the same current flows for both.

3. Results and discussion

3.1. Microstructure

Archimedes' measurements showed that the sample deposited at a process gas temperature of 900 °C (CS900) attained an average density of 7.66 g/cm^3, corresponding to 97.3 % of the theoretical bulk value. The porosity consisted of 0.3 vol. % open and 2.5 vol. % closed pores. Increasing the process gas temperature to 1000 °C (CS1000) increased the density to 7.70 g/cm^3, corresponding to 98 % of the bulk, eliminating the open porosity completely. Consistent with this trend, SEM image analysis gave porosity area fractions of 3.9 %, 2.3 %, and 3.0 % for CS900 in the L-S, L-T, and T-S sections (average $\sim$ 3.0 %), respectively, and 3.5 %, 1.4 %, and 1.8 % for CS1000 (average $\sim$ 2.2 %). The L-S sections showed the highest porosity in both deposits, indicating that the pore distribution is direction-dependent and associated with deposition tracks, inter-particle boundary networks, and weakly bonded regions. The image-based porosity values are slightly higher than Archimedes tests because 2D thresholding is sensitive to section orientation and the selected fields of view, whereas Archimedes measurements provide a bulk-average measure of total porosity [24].

By comparison to CSAM, sintered PM pure iron has been reported to achieve a compacted green density of 7.67 g/cm^3, further densifying to 7.80 g/cm^3 after sintering at 1450 °C for 1 h [5]. Even better results were obtained in a study [4] using L-PBF, where the pure iron parts exceeded 99 % relative density ($\geq$ 7.80 g/cm^3) in the as-built state. Thus, the CS1000 sample approached the density of sintered PM parts but remained below the as-built densification achieved via L-PBF.

Fig. 3 presents a pseudo-3D image compiled from SEM ECCI micrographs and EBSD IPF in different directions for both CS900 and CS1000 deposits. The CS900 contained notably more, longer inter-particle voids, whereas the CS1000 sample appeared denser, in line with the Archimedean weighing results. The IPF maps indicated a partial flattening of the particles as well as the grains, but overall, a random orientation of the grains was preserved. This is because cold spraying does not involve any melting of the input materials, so unlike laser-based AM, the material did not experience epitaxial grain growth. The microstructure at particle interfaces appears as refined, with the finest grains and highest misorientation located near the interfaces. The formation of this harmonic structure was triggered by the severe plastic deformation upon the particle impact that induced dynamic recrystallisation, which was driven by the high strain rate deformation and adiabatic local heating of the particle interfaces [25]. The dark, unindexed bands were mainly located along inter-particle boundaries, where pores and weakly bonded

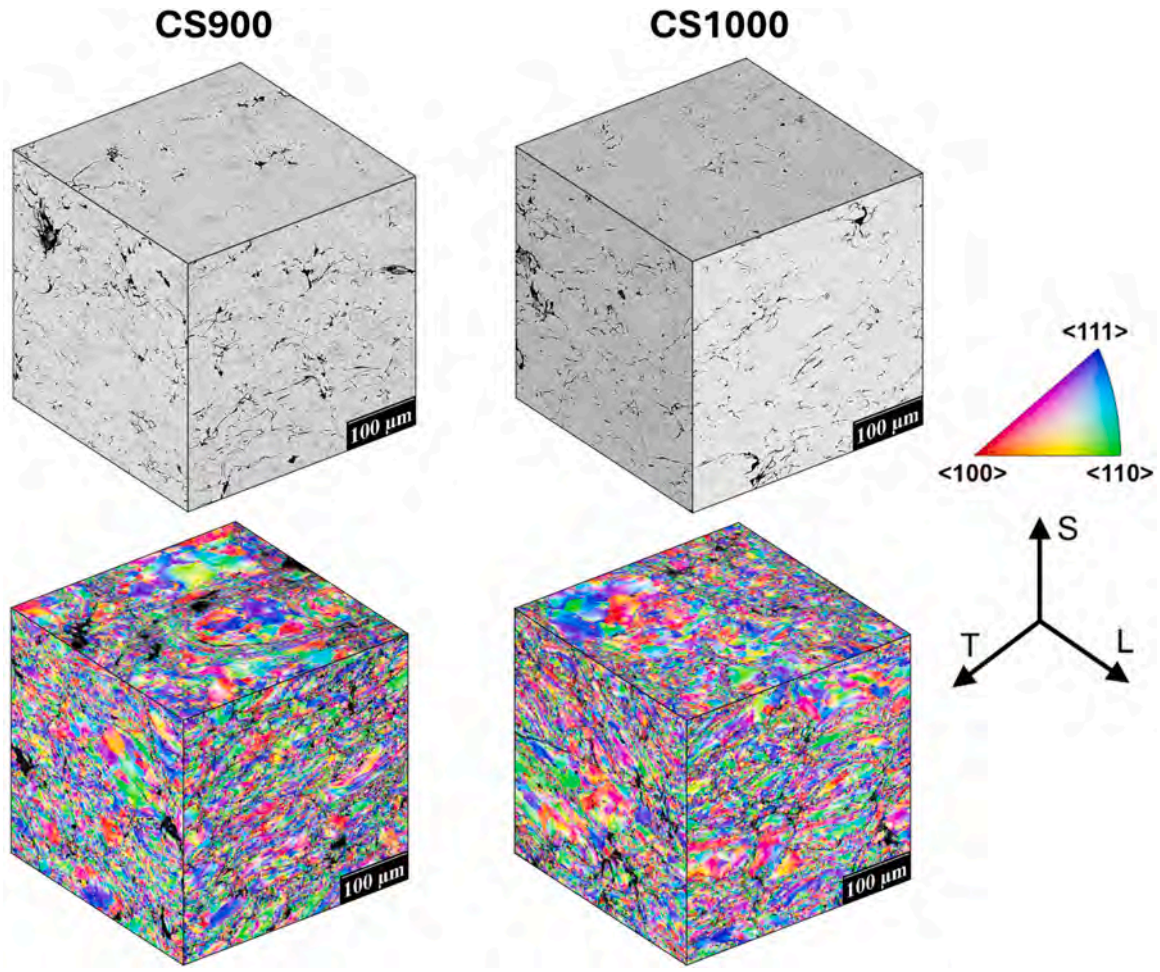

Fig. 3. Pseudo-3D microstructure of the cold-sprayed pure iron deposits produced at process gas temperatures of 900 °C and 1000 °C (SEM and EBSD IPF maps).

regions might be present. However, unindexed regions can also arise from highly deformed, ultrafine-grained interfacial zones, where high

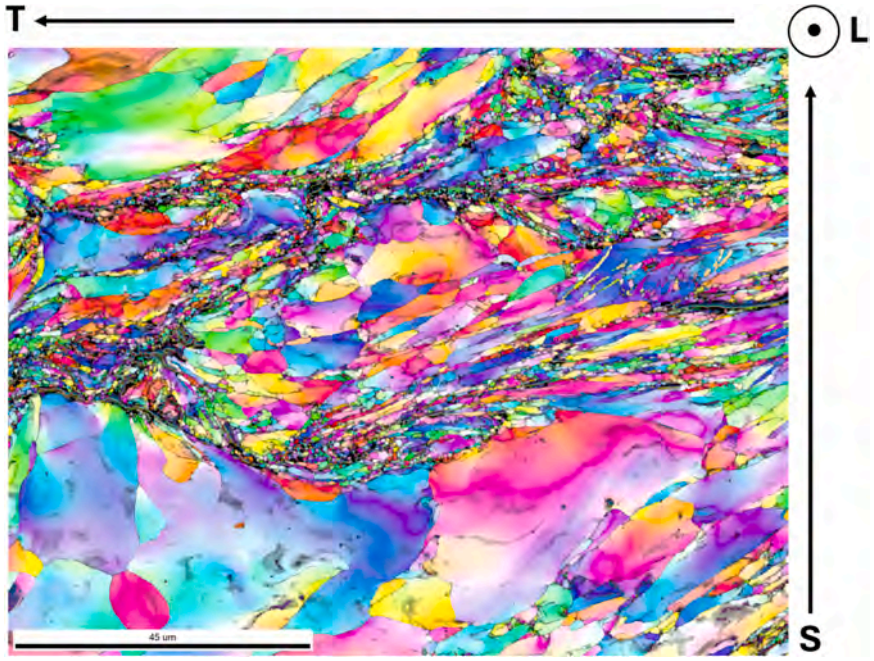

Fig. 4. Higher-magnification EBSD IPF map of the CS1000 (same IPF key as Fig. 3), showing the ultrafine-grained, highly deformed interfacial zones alongparticle boundaries.

dislocation density and very small grain size reduce EBSD pattern quality and lower indexing rates [26,27]. Fig. 4 provides a higher-magnification EBSD IPF map of the CS1000 deposit with the cross-section in the build direction (S), highlighting these interfacial zones in more detail and showing dense bands of ultrafine grains along inter-particle boundaries compared with the coarser particle interiors.

3.2. Stress-strain response, fatigue crack growth rate, and fracture toughness evaluation

Fig. 5 summarizes the results from mechanical testing. As shown in Fig. 5(a), the CS1000 achieved higher strength than the CS900 deposit; the strain to fracture being similar for both cases. The higher strength of deposits produced at higher process gas temperature was attributed to enhanced particle plastic deformation and improved inter-particle contact during impact, including a stronger tamping effect [28]. Enlarged areas of adiabatic shear instabilities caused interface bonding and improved the inter-particle cohesion [29]. In the CS1000, the L-S orientation reached the highest ultimate tensile strength (UTS) of 252 MPa, while the T-S orientation showed the maximum strain to failure of 0.253 %. Furthermore, no consistent trend among L-S, L-T, T-S, and T-L orientations appeared (Table 1), confirming that the tensile behavior in cold-sprayed pure iron is governed by residual porosity and heterogeneous distribution of non-bonded interfaces rather than by crystallographic textures or particle shapes. The CSAM pure iron achieved a UTS nearly matching its cold-rolled counterpart (~ 270 MPa UTS, ~ 49 % elongation), but with negligible ductility, whereas L-PBF pure iron exceeds a UTS of 430 MPa with over 18 % elongation [30,31]. The very low ductility of the cold-sprayed deposits can be attributed to lower inter-particle cohesion, reflected by poorly bonded inter-particle regions that act as crack nuclei, together with the heavily work-hardened particle microstructure adjacent to particle interfaces [25,32]. Under tensile loading, these hardened regions prevent deformation by restricting dislocation movement, contributing to a stress concentration at the non-bonded interfaces. Crack growth is then initiated before the material can undergo homogeneous plastic deformation, as typically exhibited in the L-PBF or cold-rolled pure iron with homogeneous stress distribution.

Similar to the results from quasi-static testing, the CS1000 also showed a higher fracture toughness than the CS900, as seen in the R-curves in Fig. 5(b) and the K_{IC} values in Table 1. However, the average K_{IC} of 18.94 MPa·m$^{0.5}$ in the CS1000 reached only about 16 % of the 132–202 MPa·m$^{0.5}$ reported for wrought pure iron with a fully dense and uniform microstructure [33]. In cold spray deposits of pure iron, cracks bypassed the particle interiors by propagating along weakly bonded particle boundaries and trapped voids, where only limited plastic deformation occurs. In contrast, crack-tip blunting occurs in wrought iron, resulting in localized plasticity at the crack front, which then requires more energy for crack propagation. Since the interfaces of CSAM deposits undergo such blunting only to a limited extent, crack propagation required less energy, resulting in much lower fracture toughness than their wrought counterparts [20].

Fig. 6 presents the FCGR as a function of maximum stress intensity factor (K_{max}) for all orientations. Final fracture morphologies attained after testing are given in Fig. 7. The CS1000 showed a higher crack propagation threshold (K_{th}) than the CS900. For CS900, the weaker inter-particle bonding, as well as the slightly higher amounts of non-bonded interfaces and porosity, provided easy crack paths in all directions. Thus, the da/dN curves pertaining to different orientations converged at around 8 MPa·m$^{0.5}$. In the CS1000, stronger bonding forces caused cracks in L-S and T-S orientations to propagate across particles, as shown in Fig. 7, raising ΔK_{th} and lowering da/dN. In L-T and T-L, cracks propagated along particle planes with less resistance. Above ~ 10 MPa·m$^{0.5}$, the crack driving force surpassed the critical interface strength, causing all CS1000 curves to converge.

The curves for both CSAM pure iron deposits showed distinct elbows, related to significant changes in the exponents, which mark a sudden increase in crack growth rate beyond the threshold region. At K_{max} values just above ΔK_{th}, cracks advanced trans-granularly through particle interiors. Once K_{max} exceeded the strength limits of internal interfaces, cracks could no longer be hindered from growth. Thus, FCGR jumps sharply as the crack propagation causes inter-particle decohesion along sequences of weak particle boundaries, producing the observed elbows in the CSAM deposit curves. The FCGR of CSAM pure iron deposits was two orders of magnitude higher than that of wrought iron in the Paris region, since wrought iron benefits from a uniform, pore-free microstructure that promotes crack-tip blunting through plastic deformation and yields the much lower growth rate over the K_{max} range [34]

Table 1 lists the constants obtained by fitting the crack-growth data to the Hartmann-Schijve model described in detail in [35,36],

$$\frac{da}{dN} = D\cdot\frac{(\Delta K - \Delta K_{thr})^p}{\left(1-\frac{K_{max}}{A}\right)^{\frac{p}{2}}}. \quad (1)$$

In this equation, ΔK_{thr} represents the FCGR threshold used in the fit. The ASTM E647 threshold ΔK_{th} (defined at da/dN =10^{-10} m/cycle) was then calculated using the equation:

$$\Delta K_{th} \approx \Delta K_{thr} + \left(\frac{10^{-10}}{D}\right)^{\frac{1}{p}}. \quad (2)$$

Also, the stress intensity factor (ΔK) was equated to K_{max} since the test was conducted at $R \sim -1$. In this fit, the same rate constant D and exponent p values were used for both the L-S and T-S orientations, while

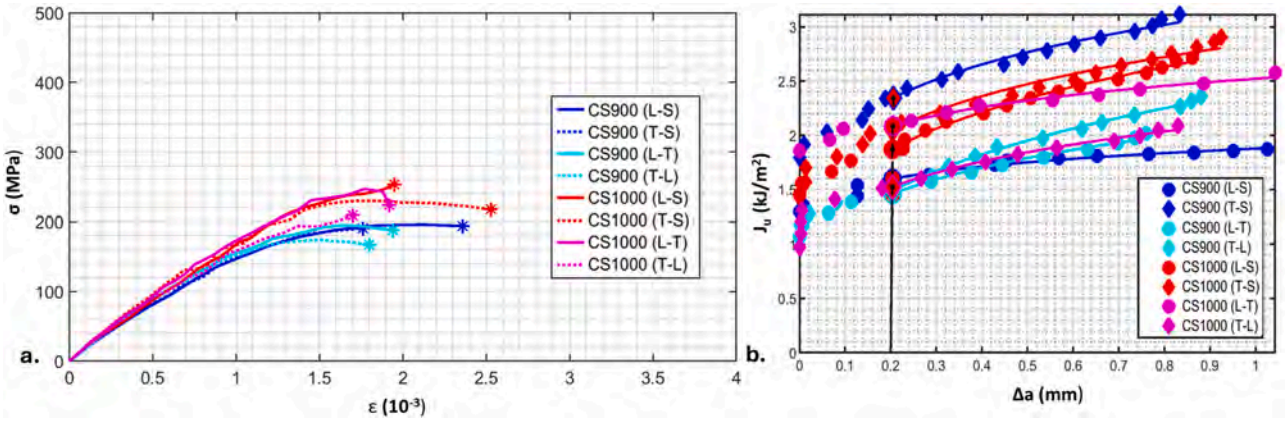

Fig. 5. (a) Stress (σ)-strain (ε) curves and (b) crack resistance (R-curve) plots showing J-integral (J_u) vs. crack extension (Δa) for CS900 and CS1000 samples with different orientations.

Table 1
Mechanical properties and fit parameters for the Hartmann-Schijve crack-growth model: D (rate constant), p (slope), ΔK_{thr} (intrinsic threshold from the fit), ΔK_{th} (ASTM-defined threshold), K_{IC} (fracture toughness assumed as A in the model), E (Young's modulus), UTS (ultimate tensile strength), and ε (total elongation).

Orientation	E (GPa)	UTS (MPa)	E ($\times 10^{-3}$)	ΔK_{th} (MPa·m$^{0.5}$)	ΔK_{thr} (MPa·m$^{0.5}$)	K_{IC} (MPa·m$^{0.5}$)	D ($\times 10^{-8}$)	p
CS900 (L-S)	176.79	196.12	2.36	4.83	4.83	16.04	12.30	1.21
CS900 (T-S)	187.43	194.90	1.94	5.44	5.44	20.30	12.30	1.21
CS900 (L-T)	178.35	190.89	1.76	4.61	4.61	15.33	8.88	1.38
CS900 (T-L)	193.39	174.03	1.80	4.81	4.8	16.16	8.88	1.38
CS1000 (L-S)	186.86	252.73	1.95	6.41	6.39	17.84	2.54	1.54
CS1000 (T-S)	202.59	246.54	1.92	6.56	6.54	19.47	2.54	1.54
CS1000 (L-T)	208.51	229.49	2.53	5.72	5.72	19.89	7.73	1.23
CS1000 (T-L)	190.25	209.28	1.70	5.53	5.52	16.24	7.73	1.23

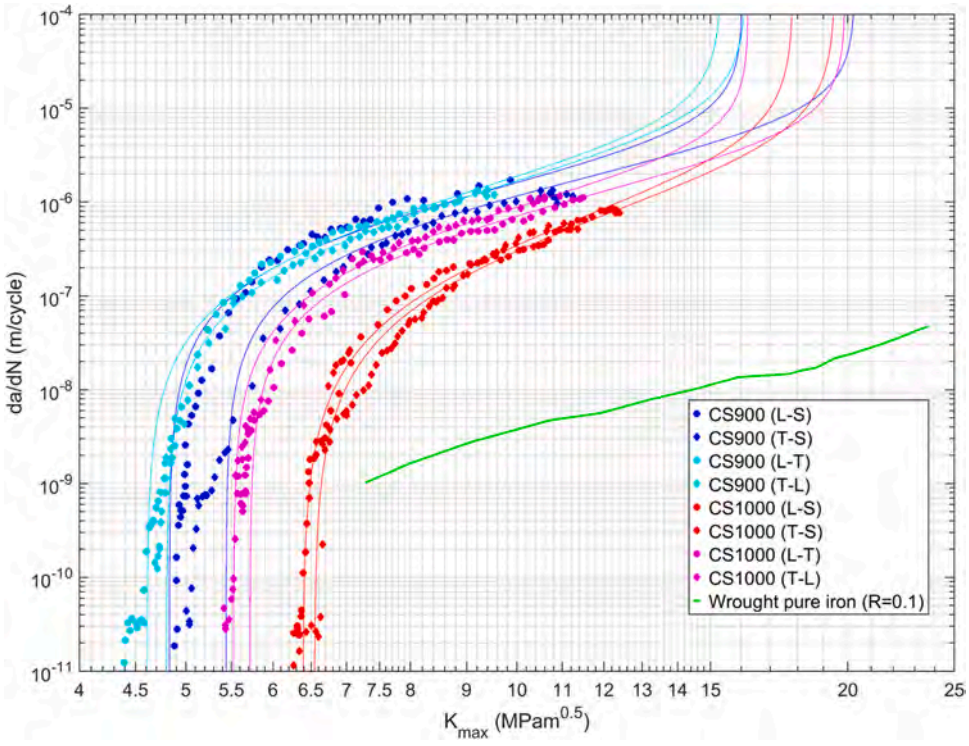

Fig. 6. FCGR (da/dN) versus maximum stress intensity factor (K_{max}) for CS900 and CS1000 pure iron samples of different orientations. FCGR data of wrought pure iron has been reconstructed from [34].

a separate pair of values was fitted to the L-T and T-L orientations. The parameter A, denoting the dynamic fracture toughness in the Hartmann-Schijve equation, was approximated here by the experimentally measured K_{IC}. The resulting fit constants D and p, together with ΔK_{thr}, K_{max}, and K_{IC}, provided a complete fracture-mechanics description of each orientation. This model was used instead of the standard Paris law as it comprehends both the near-threshold behavior (via ΔK_{thr}) and the curvature at high driving forces as K_{max} approaches the fracture toughness A, whereas the Paris law is limited to the mid-range power-law regime.

4. Fractographic observations

Out of the four in-plane orientations (L-S, L-T, T-S, T-L), only the L-S and L-T specimens were examined by fractography to reveal reasons for the anisotropies shown during testing by FCGR. The data of the other combinations already confirmed transverse isotropy. As illustrated in Fig. 7, in the CS900 deposit, both L-S and L-T orientations displayed trans-granular cleavage at near-threshold loading. Once K_{max} entered the Paris regime and into the quasi-static fracture region, crack propagation shifted entirely to inter-particle decohesion. In the CS1000, L-S and L-T also fractured trans-granularly at near-threshold, although the L-S facets appeared relatively flat because the crack advancing along the S direction met the L-T oriented interfaces nearly normal. So, the local loading was Mode I tensile (opening), and the crack cut occurs across the short axis of the flattened particles. In L-T orientation, the crack propagated along the T direction, where flattened particles appeared as rounded cross-sections. It passed the interfaces at shallow angles, carried a larger shear component (mixed mode), and glided along curved boundaries, producing stepped facets. In the Paris regime, the CS1000 (L-S) sample showed a mixture of trans-granular and trans-particle features, whereas CS1000 (L-T) exhibited predominantly inter-particle decohesion. Under quasi-static loading, both orientations showed inter-particle separation with some ductile dimples. By comparison, wrought pure iron when subjected to fatigue shows only uniform, striation-like ductile features and fully trans-granular fracture across the entire ΔK range [37,38].

5. Magnetic and electrical properties

The DC B-H hysteresis loops provided in Fig. 8 show that the CS1000 pure iron deposit is magnetically slightly harder than the reference of a cold-drawn low-carbon steel bar. Since the cylindrical specimens were extracted with their longitudinal axis aligned with the L-direction and

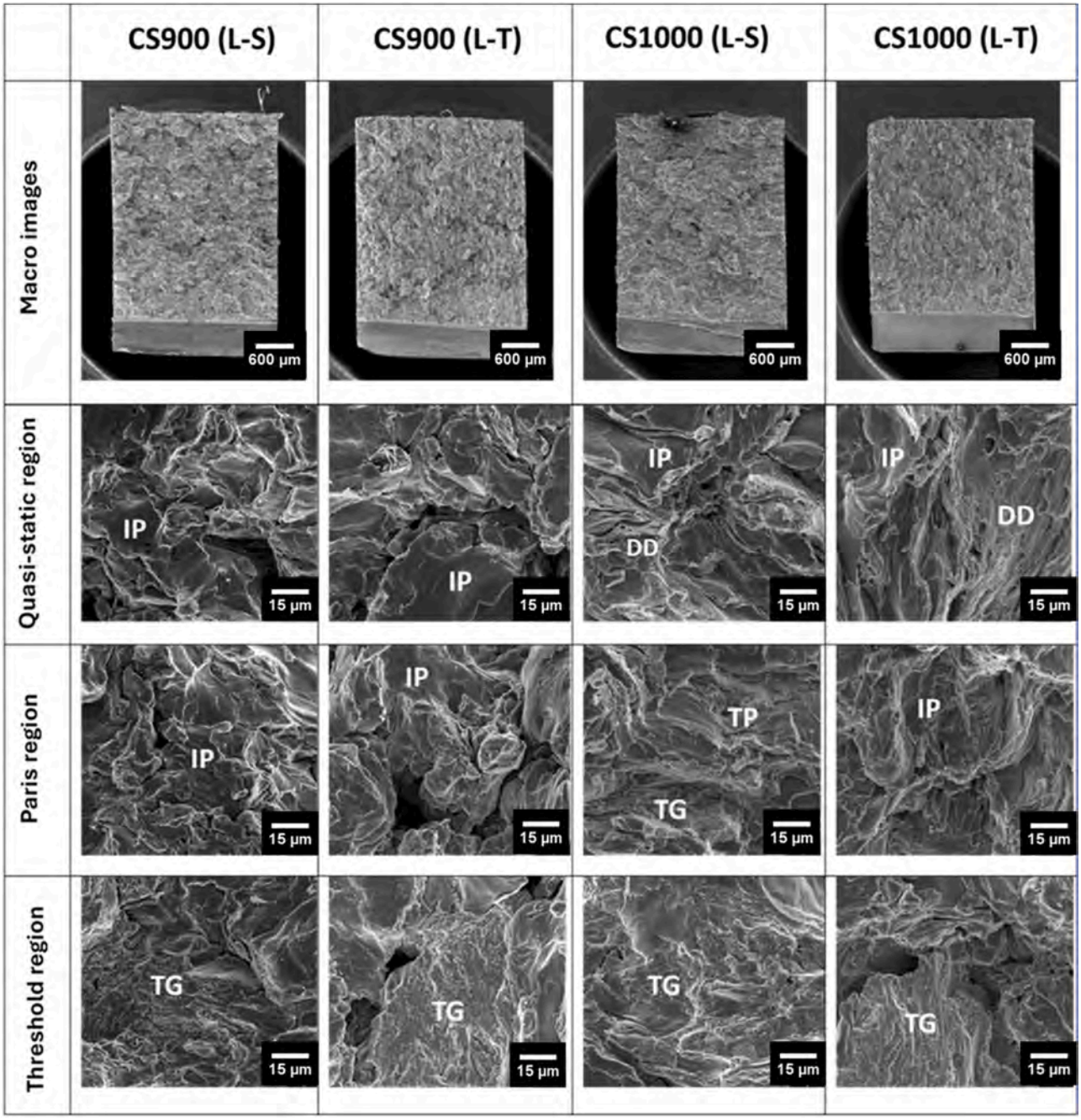

Fig. 7. Fractography of CS900 and CS1000 pure iron deposits for L-S and L-T orientations under near-threshold, Paris-region, and quasi-static loading. IP = inter-particle decohesion, DD = ductile dimples, TP = trans-particle fracture, TG = trans-granular fracture.

were measured with the magnetic field applied along this axis, the reported values correspond to this orientation. Cold-sprayed deposits comprise plastically deformed particles joined across inter-particle interfaces, with those interfaces stacked predominantly along the S-direction. Consistent with the higher porosity measured via SEM image analysis in the L-S sections, the magnetic response is expected to vary with the field direction. Applying the field along the S-direction, which intersects a higher fraction of inter-particle interfaces, would be expected to reduce permeability and increase coercivity [39]. Quantification of this anisotropy was not performed in this study.

As quantified from the measured B-H data, the CSAM specimen saturated at only 0.16 T (versus 1.02 T for the steel), and its maximum relative permeability peaked at 52, compared to 170. The CS deposit showed a slightly higher coercivity (91 A/m versus 74 A/m), and its specific hysteresis losses reach 323.6 J/m^3 (cf. 181.4 J/m^3 for the bulk steel). Similar limitations in the as-sprayed magnetic response of cold-sprayed soft-magnetic deposits have been reported in the literature and are attributed to micro-pores, inter-particle boundaries, and deformation-induced defects such as residual stress, dislocations, and grain refinement [40]. In the CSAM pure iron, the non-bonded interfaces and porosities could act as domain wall-pinning sites and prevent the uniform rotation and translation of magnetic domains. Also, the work-hardened boundary areas of individual particles provided minimal soft magnetic regions to support domain rotation, further reducing permeability. In our previous paper [41], we demonstrated via positron annihilation spectroscopy that these interfacial regions in CS deposits have higher dislocation densities along with the presence of vacancy clusters, which are not observed in cold-rolled pure metals. According to

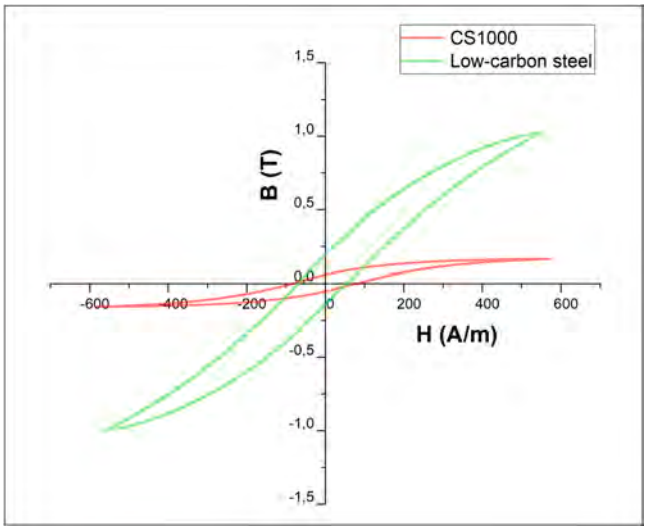

Fig. 8. Comparison of the hysteresis curves of CS1000 and cold-drawn low-carbon steel bar.

the domain-wall pinning theory [42], these defects act as highly effective pinning centers, driving the increased coercivity and reduced permeability observed in CS pure iron deposits.

Literature reports the resistivity of high-purity bulk iron at room temperature to be about 97 nΩ·m [43]. The DC resistivity of the CS1000 pure iron deposit was determined as 156 nΩ·m, compared to 160 nΩ·m for the tested cold-rolled low-carbon steel bar. In the case of the steel specimen, the presence of alloying elements such as carbon, manganese, and silicon further increases resistivity compared with pure iron, owing to impurity scattering. The higher value for CSAM iron can be attributed to enhanced electron scattering at pores, inter-particle boundaries, and the high dislocation/vacancy densities introduced during CSAM. Nevertheless, the measured resistivity of CSAM iron was practically identical to that of the low-carbon steel.

Despite these limitations, cold spraying of pure iron deposits still offers electromagnetic functionality for precise, oxidation-free repair and additive manufacturing for soft-magnetic applications. Its ability to locally restore geometrical integrity and functionality without thermal damage makes it an effective solution for targeted maintenance and specialized applications. Unlike load-bearing applications, mechanical properties and damage tolerance are not critically required here. Apart from that, most of the here-revealed dependencies should be transferable to other highly deformable ferritic alloys, allowing for a broader range of applications.

6. Conclusion

This work demonstrated that cold spraying can be used to produce dense, soft-magnetic ferritic deposits suitable for additive manufacturing and repair applications by using pure iron as a model system. Raising the nitrogen process gas temperature from 900 °C to 1000 °C increased the relative density to 98 % and raised the ultimate tensile strength from 196 to 252 MPa. Porosity and the presence of non-bonded interfaces between particle splats result in limited ductility and fracture toughness while accelerating fatigue crack growth. Cracks propagated by trans-particle mode near ΔK_{th} and by inter-particle decohesion at higher K_{max}. Magnetic tests showed a saturation induction of 0.16 T and a relative permeability of 52; both lower than those given for wrought low-carbon steel. The coercivity (91 A/m) and hysteresis losses (324 J/m^3) of the deposits were higher than those of the cold-drawn low-carbon steel, while electrical resistivity (156 nΩ·m) was similar. Despite these shortcomings, cold-sprayed pure iron deposits can still provide sufficient flux capacity for low-field, low-frequency/DC service, making it a cost-effective, oxidation-free option for repairing damaged magnetic components instead of scrapping them. It is also ideal for the fabrication of functional deposits where peak magnetic performance is not required. For applications requiring higher magnetic performance, future work should focus on post-spray annealing and the use of alloyed ferritic powders (e.g., Fe-Si or Fe-Al).

CRediT authorship contribution statement

Abhinav Anand: Writing – original draft, Investigation, Formal analysis, Data curation, Conceptualization. **Ondřej Kovářík:** Writing – review & editing, Methodology, Investigation, Formal analysis. **Pavel Ctibor:** Writing – original draft, Investigation, Data curation. **Zahra Arabgol:** Writing – review & editing, Investigation. **Levke Wiehler:** Writing – review & editing, Investigation. **Frank Gärtner:** Writing – review & editing, Writing – original draft, Investigation. **Thomas Klassen:** Resources, Conceptualization. **Jan Cizek:** Writing – review & editing, Supervision, Resources, Funding acquisition, Conceptualization.

Declaration of competing interest

The authors declare that they have no known competing financial interests or personal relationships that could have appeared to influence the work reported in this paper.

Acknowledgement

The authors thank Petr Králíček (Institute of Plasma Physics, Czechia) for assistance during the cold spray deposition. The help of Dr. Josef Sedláček (Faculty of Electrical Engineering, CTU Prague) at the adjustment of the resistivity test is also acknowledged. The PhD thesis of Abhinav Anand has been funded by the EU/Horizon/Doctoral Networks/Marie Skłodowska-Curie grant agreement No 101119988. The Czech Science Foundation project 22-14048S and project FerrMion of the Ministry of Education, Youth, and Sports of the Czech Republic, co-funded by the European Union (CZ.02.01.01/00/22_008/0004591), are gratefully acknowledged.

Supplementary materials

Supplementary material associated with this article can be found, in the online version, at doi:10.1016/j.addlet.2026.100363.

Data availability

Data will be made available on request.

References

[1] Y. Tang, S. Liu, S. Li, R. Ma, Y. Li, K. Wang, M. Fang, C. Zhou, S. Yang, Y. Zhang, A review of artificial intelligence-driven innovations in soft magnetic materials optimization: current trends and future horizons, MetalMat 2 (2025) e70001, https://doi.org/10.1002/metm.70001.

[2] C.-W. Lu, F.-Y. Hung, T.-W. Chang, H.-Y. Hsieh, Study and application on the electromagnetic stainless steel: microstructure, tensile mechanical behavior, and magnetic properties, Materials (Basel) 17 (2024), https://doi.org/10.3390/ma17122998.

[3] M. Imura, Induction cookware with ferromagnetic coating and coating method, WO2006050490A2, https://patents.google.com/patent/WO2006050490A9/en, 2006.

[4] M. Zanni, L. Ceschini, A. Fortunato, G. Valli, L. Del Bianco, F. Spizzo, Relationship between microstructure, mechanical and magnetic properties of pure iron produced by laser powder bed fusion (L-PBF) in the as-built and stress relieved conditions, Prog. Addit. Manuf. 7 (2022) 1195–1212, https://doi.org/10.1007/s40964-022-00294-7.

[5] J. Ma, M. Qin, X. Zhang, L. Zhang, X. Qu, L. Tian, Microstructure and magnetic properties of high density P/M pure iron, Mater. Res. Bull. 64 (2015) 123–127, https://doi.org/10.1016/j.materresbull.2014.12.039.

[6] E. Rúa Ramírez, A. Silvello, E.T. Diaz, R.F. Vaz, I.Garcia Cano, Reusing 316L stainless steel feedstock powder for cold spray deposition, J. Therm. Spray Technol. 34 (2025) 75–87, https://doi.org/10.1007/s11666-024-01884-3.

[7] R.F. Vaz, V. Albaladejo-Fuentes, J. Sanchez, U. Ocaña, Z.G. Corral, H. Canales, I. G. Cano, Metal knitting: a new strategy for cold gas spray additive manufacturing, Materials (Basel) 15 (2022), https://doi.org/10.3390/ma15196785.

[8] H. Hammouda, S. Msolli, N. Feninechе, H. Liao, O. Marconot, S. Deng, Magnetic performance and microstructural characterization of cold sprayed ferromagnetic materials, in: 2025: pp. 87–92. https://doi.org/10.31399/asm.cp.itsc2025p0087.

[9] N. Satpute, P. Dhoka, M. Iwaniec, S. Jabade, P. Karande, Manufacturing of pure iron by cold rolling and investigation for application in magnetic flux shielding, Materials (Basel) 15 (2022), https://doi.org/10.3390/ma15072630.

[10] S. Yin, P. Cavaliere, B. Aldwell, R. Jenkins, H. Liao, W. Li, R. Lupoi, Cold spray additive manufacturing and repair: fundamentals and applications, Addit. Manuf. 21 (2018) 628–650, https://doi.org/10.1016/j.addma.2018.04.017.

[11] J. Cizek, O. Kovarik, J. Cupera, J. Kondas, T. Bajer, F. Siska, M. Janovska, H. Seiner, Measurement of mechanical and fatigue properties using unified, simple-geometry specimens: cold spray additively manufactured pure metals, Surf. Coat. Technol. 412 (2021), https://doi.org/10.1016/j.surfcoat.2021.126929.

[12] H. Herbert, Ueber den Zusammenhang der Biegungselastizität des Gußeisens mit seiner Zug- und Druckelastizität. Forschungsarbeiten Auf Dem Gebiete Des Ingenieurwesens: Insbesondere Aus Den Laboratorien Der Technischen Hochschulen, Springer Berlin Heidelberg, Berlin, Heidelberg, 1910, pp. 39–81, https://doi.org/10.1007/978-3-662-02218-4_2.

[13] E08 Committee, Test method for measurement of fracture toughness, West Conshohocken, PA, 2019.

[14] E08 Committee, Test method for measurement of fatigue crack growth rates, West Conshohocken, PA, 2016.

[15] R.F. Vaz, A. Silvello, J. Sanchez, V. Albaladejo, I. García-Cano, The influence of the powder characteristics on 316l stainless steel coatings sprayed by cold gas spray, Coatings 11 (2021) 1–18, https://doi.org/10.3390/coatings11020168.

[16] J.W. Murray, M.V. Zuccoli, T. Hussain, Heat treatment of cold-sprayed C355 al for repair: microstructure and mechanical properties, J. Therm. Spray Technol. 27 (2018) 159–168, https://doi.org/10.1007/s11666-017-0665-z.

[17] J. Schmitt, J. Fiebig, S. Schrüfer, O. Guillon, R. Vaßen, Adjusting residual stresses during cold spray deposition of IN718, J. Therm. Spray Technol. 33 (2024) 210–220, https://doi.org/10.1007/s11666-023-01673-4.

[18] J. Pattison, S. Celotto, A. Khan, W. O'Neill, Standoff distance and bow shock phenomena in the cold spray process, Surf. Coat. Technol. 202 (2008) 1443–1454, https://doi.org/10.1016/j.surfcoat.2007.06.065.

[19] E08 Committee, Test method for linear-elastic plane-strain fracture toughness of metallic materials, West Conshohocken, PA, 2022.

[20] O. Kovářík, J. Siegl, J. Cizek, T. Chraska, J. Kondas, Fracture toughness of cold sprayed pure metals, J. Therm. Spray Technol. 29 (2019), https://doi.org/10.1007/s11666-019-00956-z.

[21] J. Blaber, B. Adair, A. Antoniou, Ncorr: open-source 2D digital image correlation matlab software, Exp. Mech. 55 (2015) 1105–1122, https://doi.org/10.1007/s11340-015-0009-1.

[22] C.A. Schneider, W.S. Rasband, K.W. Eliceiri, NIH image to imageJ: 25 years of image analysis, Nat. Methods 9 (2012) 671–675, https://doi.org/10.1038/nmeth.2089.

[23] O. Kovářík, Differential compliance from time domain vibration waveform fit and its application to fatigue crack growth rate testing, Int. J. Fract. 249 (2025) 67, https://doi.org/10.1007/s10704-025-00881-z.

[24] T. de Terris, O. Andreau, P. Peyre, F. Adamski, I. Koutiri, C. Gorny, C. Dupuy, Optimization and comparison of porosity rate measurement methods of Selective Laser Melted metallic parts, Addit. Manuf. 28 (2019) 802–813, https://doi.org/10.1016/j.addma.2019.05.035.

[25] Y. Zou, Cold spray additive manufacturing: microstructure evolution and bonding features, Acc. Mater. Res. 2 (2021) 1071–1081, https://doi.org/10.1021/accountsmr.1c00138.

[26] P.W. Trimby, Y. Cao, Z. Chen, S. Han, K.J. Hemker, J. Lian, X. Liao, P. Rottmann, S. Samudrala, J. Sun, J.T. Wang, J. Wheeler, J.M. Cairney, Characterizing deformed ultrafine-grained and nanocrystalline materials using transmission Kikuchi diffraction in a scanning electron microscope, Acta Mater. 62 (2014) 69–80, https://doi.org/10.1016/j.actamat.2013.09.026.

[27] L. Yang, P. Wang, X. Luo, H. Li, H. Yang, S. Wang, Q. Li, Nanocrystallization of interfacial microstructure of deformed particles in cold sprayed Ti6Al4V deposits, Mater. Des. 210 (2021) 110117, https://doi.org/10.1016/j.matdes.2021.110117.

[28] M.F. Morks, S.H. Zahiri, X.-B. Chen, S. Gulizia, A. Vargas-Uscategui, I.S. Cole, Influence of gas temperature and heat treatment on microstructure and properties of cold sprayed commercially pure titanium, J. Mater. Eng. Perform. 31 (2022) 5549–5558, https://doi.org/10.1007/s11665-022-06621-x.

[29] F. Gärtner, T. Stoltenhoff, J. Voyer, H. Kreye, S. Riekehr, M. Koçak, Mechanical properties of cold-sprayed and thermally sprayed copper coatings, Surf. Coat. Technol. 200 (2006) 6770–6782, https://doi.org/10.1016/j.surfcoat.2005.10.007.

[30] P. Lejček, J. Čapek, M. Roudnická, O. Molnárová, J. Maňák, J. Duchoň, D. Dvorský, M. Koller, H. Seiner, P. Svora, D. Vojtěch, Selective laser melting of iron: multiscale characterization of mechanical properties, Mater. Sci. Eng. A 800 (2021), https://doi.org/10.1016/j.msea.2020.140316.

[31] C.S. Obayi, R. Tolouei, A. Mostavan, C. Paternoster, S. Turgeon, B.A. Okorie, D. O. Obikwelu, D. Mantovani, Effect of grain sizes on mechanical properties and biodegradation behavior of pure iron for cardiovascular stent application, Biomatter. 6 (2016) e959874, https://doi.org/10.4161/21592527.2014.959874.

[32] C. Borchers, F. Gärtner, T. Stoltenhoff, H. Assadi, H. Kreye, Microstructural and macroscopic properties of cold sprayed copper coatings, J. Appl. Phys. 93 (2003) 10064–10070, https://doi.org/10.1063/1.1573740.

[33] M. Srinivas, G. Malakondaiah, R.W. Armstrong, P.R. Rao, Ductile fracture toughness of polycrystalline armco iron of varying grain size, 1991.

[34] T. Shinko, G. Hénaff, D. Halm, G. Benoit, H. Bahsoun, Characteristic dependency of hydrogen-affected fatigue crack growth and crack tip plasticity on low loading frequency in α-Iron, Metall. Mater. Trans. a Phys. Metall. Mater. Sci. 51 (2020) 4313–4326, https://doi.org/10.1007/s11661-020-05860-8.

[35] K.-H. Schwalbe, On the beauty of analytical models for fatigue crack propagation and fracture—A personal historical review, J. ASTM. Int. 7 (2010) JAI102713.

[36] O. Kovarik, J. Cizek, J. Klecka, Fatigue crack growth rate description of RF-plasma-sprayed refractory metals and alloys, Materials (Basel) 16 (2023), https://doi.org/10.3390/ma16041713.

[37] Birenis Domas, Ogawa Yuhei, Matsunaga Hisao, Takakuwa Osamu, Yamabe Junichiro, Prytz Øystein, Thøgersen Annett, Hydrogen-assisted fatigue crack propagation in a pure BCC iron. Part II: accelerated regime manifested by quasi-cleavage fracture at relatively high stress intensity range values, MATEC Web Conf. 165 (2018) 3010, https://doi.org/10.1051/matecconf/201816503010.

[38] D. Birenis, Y. Ogawa, H. Matsunaga, O. Takakuwa, J. Yamabe, Ø. Prytz, A. Thøgersen, Interpretation of hydrogen-assisted fatigue crack propagation in BCC iron based on dislocation structure evolution around the crack wake, Acta Mater. 156 (2018) 245–253, https://doi.org/10.1016/j.actamat.2018.06.041.

[39] F. Ternero, L.G. Rosa, P. Urban, J.M. Montes, F.G. Cuevas, Influence of the total porosity on the properties of sintered materials—a review, Metals. (Basel) 11 (2021), https://doi.org/10.3390/met11050730.

[40] X. Xie, C. Chen, Y. Ma, Y. Xie, H. Wu, G. Ji, E. Aubry, Z. Ren, H. Liao, Influence of annealing treatment on microstructure and magnetic properties of cold sprayed Ni-coated FeSiAl soft magnetic composite coating, Surf. Coat. Technol. 374 (2019) 476–484, https://doi.org/10.1016/j.surfcoat.2019.05.008.

[41] J. Cizek, J. Medricky, F. Stefanik, F. Lukac, J. Cupera, J. Kondas, R. Singh, O. Melikhova, P. Hruska, J. Cizek, Cold sprayed deposits characterized by positron annihilation spectroscopy, J. Therm. Spray Technol. 33 (2024) 666–675, https://doi.org/10.1007/s11666-024-01763-x.

[42] A.R. All, Z.M. Farid, E. Takla, The effect of lattice disorders on domain wall-dislocation interaction in Ni-5wt% Mn alloy, 1992.

[43] J.D. Cutnell, K.W. Johnson, D. Young, S. Stadler, Physics, Wiley, 2021, 12th ed.